Journal of Biomedical Materials Research Part B: Applied Biomaterials

Designing new biocompatible glass-forming Ti75-xZr10NbxSi15 (x= 0, 15) alloys: corrosion, passivity and apatite formation

Journal:	*Journal of Biomedical Materials Research: Part B - Applied Biomaterials*
Manuscript ID:	JBMR-B-14-0428.R1
Wiley - Manuscript type:	Original Research Report
Date Submitted by the Author:	06-Oct-2014
Complete List of Authors:	Abdi, Somayeh; IFW Institute, Institute for Complex Materials Oswald, Steffen; IFW Institute, Complex Materials Gostin, Petre; IFW Institute, Complex Materials Helth, Arne; IFW Institute, Complex Materials Sort, Jordi; Univ Autonoma Barcelona, Physics department Baró, Dolors; Universitat Autonoma de Barcelona, Fisica de Materials II Calin, Mariana; IFW Institute, Complex Materials Schultz, Ludwig; IFW Institute, Metallic Materials Eckert, Jürgen; IFW Institute, Complex Materials Gebert, Annett; IFW Institute, Complex Materials
Keywords:	corrosion, implant design, calcium phosphate(s), titanium (alloys), Microstructure

Designing new biocompatible glass-forming $Ti_{75-x}Zr_{10}Nb_xSi_{15}$ (x= 0, 15) alloys: corrosion, passivity and apatite formation

Somayeh Abdi[1*, 2], Steffen Oswald[1], Petre Flaviu Gostin[1], Arne Helth[1,2], Jordi Sort[3], Maria Dolors Baró[4], Mariana Calin[1], Ludwig Schultz[1,2], Jürgen Eckert[1,2], Annett Gebert[1]

[1] IFW Dresden, P.O. Box 270116, D-01171 Dresden, Germany

[2] TU Dresden, Institut für Werkstoffwissenschaft, D-01062 Dresden, Germany

[3] Institució Catalana de Recerca i Estudis Avançats and Departament de Física, Facultat de Ciències, Universitat Autònoma de Barcelona, E-08193 Bellaterra, Spain

[4] Departament de Física, Facultat de Ciències, Universitat Autònoma de Barcelona, E-08193 Bellaterra, Spain

Abstract

Glass-forming Ti-based alloys are considered as potential new materials for implant applications. $Ti_{75}Zr_{10}Si_{15}$ and $Ti_{60}Zr_{10}Nb_{15}Si_{15}$ alloys (free of cytotoxic elements) can be produced as melt-spun ribbons with glassy matrix and embedded single β-type nanocrystals. The corrosion and passivation behavior of these alloys in their homogenized melt-spun states have been investigated in Ringer solution at 37°C in comparison to their cast multiphase crystalline counterparts and to cp-Ti and β-type Ti-40Nb. All tested materials showed very low corrosion rates as expressed in corrosion current densities i_{corr} <50 nA/cm². Electrochemical and surface analytical studies revealed a high stability of the new alloys passive states in a wide potential range. This corresponds to low passive current densities i_{pass} = 2±1 μA/cm² based on the growth

of oxide films with thickness d <10 nm. A homogeneous constituent distribution in the melt-spun alloys is beneficial for stable surface passivity. The addition of Nb does not only improve the glass-forming ability and the mechanical properties but also supports a high pitting resistance even at extreme anodic polarization up to 4V vs. SCE were oxide thickness values of d~35 nm are reached. With regard to the corrosion properties, the Nb-containing nearly single-phase glassy alloy can compete with the β-type Ti-40Nb alloy. SBF tests confirmed the ability for formation of hydroxyapatite on the melt-spun alloy surfaces. All these properties recommend the new glass-forming alloys for application as wear- and corrosion-resistant coating materials for implants.

Keywords. : Ti alloy, metallic glass, implant, corrosion, XPS, AES, Ringer solution

*Corresponding author. S. Abdi; Tel.: +49 351 4659 749; fax: +49 351 4659 452. Postal address: Helmholtzstrasse 20, 01069, Dresden, Germany.

E-mail address: s.abdi@ifw-dresden.de

1. Introduction

Since the middle of the 20th century, Ti and Ti-based alloys have been considered as non-degradable implant materials for load-bearing applications, such as hard tissue replacements and bone fracture healing. Meanwhile, cp-Ti and (α + β)-type Ti-6Al-4V are widely used and developed due to their very good biomechanical properties, appropriate corrosion resistance and biocompatibility in comparison with other materials such as stainless steel and Co-Cr alloys [1,2]. However, in practice also several problems were identified like low wear resistance, too high stiffness and limited strength as well as releases of toxic elements (Al, V) in biological environments which explain the need for new alloy developments [1,3].

A new generation of prospective implant materials with improved properties are β-type Ti-based alloys with significantly reduced elastic modulus (Young's modulus), which are composed only of non-toxic elements [4]. A typical example is the metastable Ti-Nb alloy system with minimum Young's modulus values of ~60-65 GPa at 40-50 wt.-% Nb, strength values up to 1000 MPa and very high corrosion resistance explained by a significant fraction of Nb oxides in the spontaneously forming passive film [5-7].

Besides that, Ti-based metallic glass-forming alloys are also attracting increasing interest as potential biomaterials as they exhibit superior mechanical properties relative to their crystalline counterparts and to conventional Ti-based materials such as very high strength (1800–2500 MPa), relatively low Young's modulus values (80-110 GPa), low density and higher wear resistance [8-13]. Typical alloy systems with bulk glass-forming ability are for example $Ti_{40}Zr_{10}Cu_{36}Pd_{14}$ with max. cast rod diameter of 6 mm [14] or $Ti_{40}Zr_{25}Cu_{12}Ni_3Be_{20}$ with max. cast rod diameter of 14 mm [15].

However, biomedical application of these alloys is restricted by the presence of cytotoxic or allergic elements such as Al, Ni, Be and Cu [16,17] in their composition which could be released as ions or metal particles from metal implants into the body tissue. This release could take place through procedures such as corrosion (stress corrosion, fatigue corrosion) or wear processes [18]. Therefore, not only the life-time of an implant depends on the corrosion resistance of the metallic material but also, the corrosion products releasing to the surrounding tissues may result in biocompatibility problems, i.e. affect cell metabolism [19-21]. Consequently, with regard to corrosion stability and related metal ion release, the use of non-toxic elements which support stable passivity must have priority in the development of new glass-forming biomaterials.

There is already clear evidence that for VM-Cu-based (VM=valve metal, i.e. Ti, Zr, Al, Ta ...) bulk glassy alloy samples local corrosion events (pitting) typically occur under massive ion release. Those corrosion events are often due to the presence of cast defects (e.g. crystalline inclusions, pores) or of defects generated by mechanical processing (e.g. shear-bands) that cause a local break down of passivity [22,23]. The first corrosion investigations of VM-Cu-based bulk metallic glasses such as in the Ti-Zr-Cu-Pd system in simulated body fluid revealed the presence of large fractions of Cu in the alloy (≥30 at.-%) as being critical for the initiation of pronounced pitting events [10,14,24]. Such a critical role of Cu for the pitting susceptibility of metallic glasses was recently confirmed in a study by Lin et al. [3] who compared the electrochemical behavior of different metallic glasses on Zr-, Ti- and Ta-base in Hanks solution.

Recently, the authors developed new glass-forming Ti-Zr-(Nb)-Si alloys which are completely free of cytotoxic elements. These alloys are considered to have a promising potential for implant applications. This has been so far derived from detailed investigations regarding microstructural and mechanical aspects [16,25]. Both melt-spun alloys $Ti_{75}Zr_{10}Si_{15}$ and $Ti_{60}Zr_{10}Nb_{15}Si_{15}$ exhibit an interesting combination of very high hardness (H) suggesting very high wear resistance and reduced elastic modulus (E_r) values which are in the order of those for crystalline Ti-based alloys [25]. For long-term use as implant material in the human body, it is essential to assess the corrosion properties of those new alloys in comparison to other potentials materials, i.e. single phase α-Ti or β-Ti-40Nb. This is the aim of the study reported in this paper. It is of fundamental importance to clarify how the alloy microstructure which is homogenized by the melt-spinning process (rapid solidification) relative to the very heterogeneous state after casting (slow cooling) as well as the alloy constituents determine

the corrosion behavior in a biologically relevant environment. It is well-known that glass-forming alloys are expected to show improved corrosion behavior in comparison with their crystalline counterparts considering their chemically homogeneous single-phase nature, and the lack of structural defects such as dislocations and grain boundaries which results in more homogenous and protective passive film on the surface [26].

In the present work, we studied the anodic polarization behavior and the oxide film growth on surfaces of glass-forming $Ti_{75-x}Zr_{10}Nb_xSi_{15}$ (x= 0, 15) alloy samples in the nearly homogenized state with glassy matrix phase and embedded nanocrystals as obtained after rapid cooling (melt-spinning) and in the (heterogeneous) multiphase micro-crystalline state that was established after slow cooling (casting) in Ringer solution. Competing implant materials, α-Ti or β-Ti-40Nb, were used as reference materials. The mechanism of passive film growth on the newly developed alloys has been investigated. The particular role of Nb in the growth of passive films and the consequences for the passive film properties will be discussed. Finally, with an SBF test the ability to form bone-like hydroxyapatite on the melt-spun alloy surfaces was evaluated.

2. Materials and methods

2.1. Materials

Ingots of nominal compositions $Ti_{75}Zr_{10}Si_{15}$ and $Ti_{60}Zr_{10}Nb_{15}Si_{15}$ (at.-%) were produced by arc-melting a mixture of the constituent elements with high purity (99.9%) in an Ar atmosphere. In order to achieve maximum chemical homogeneity, the ingots were re-melted 5 times. Rod samples with 4 mm diameter and 50 mm length were prepared by copper mold

casting (cooling rate ~1-10^3 K/s). Test samples were cut into discs with 3 mm thickness. Ribbons with 30-50 μm thickness and 3-4 mm width were prepared by melt-spinning in an Ar atmosphere using a melt temperature of 1993 K and a single-roller Cu-wheel at a rotation speed of 35 m/sec (cooling rate ~10^6 K/s). Details of sample preparation and characterization are given in [25]. As reference materials, we used rods' of high purity elements, i.e. cp-Ti (ARA-T Advance GmbH), Nb and Zr (Goodfellow). Also the single-phase β-type alloy Ti-40Nb (wt.-%) ($Ti_{74.4}Nb_{25.6}$ at.-%) was employed, which was obtained by casting rods with 8 mm diameter and subsequent homogenization treatment at 1000°C for 24 hours. Details of alloy preparation and microstructure characterization are given in [6].

The microstructure of alloy rod and ribbon samples was investigated using X-ray diffraction (XRD, D3290 PANalytical X'pert PRO with Co-Kα radiation) as well as high resolution scanning electron microscopy (HRSEM, Gemini 1530 microscope) and transmission electron microscopy (TEM: Philips TEKNAI F30 microscope, 300 kV).

2.2.Electrochemical studies

For potentiodynamic studies, rod samples were electrically connected to an isolated wire and then embedded in epoxy resin. The surfaces of the cross-sections were finished by grinding with emery SiC paper (mesh from 400 down to 2500), followed by fine-polishing with a mixture of 90% 40 nm SiO_2 suspension and 10% H_2O_2. The samples were sequentially cleaned with ethanol and bi-distilled water in an ultrasonic bath and dried in air. Melt-spun ribbons were cut in proper length of about 50 mm, cleaned carefully with ethanol and bi-distilled water then dried in air. They have been electrically connected through a metal clip and an isolated wire.

Potentiodynamic and potentiostatic polarization tests have been performed by means of a Solartron SI 1287 electrochemical interface which was connected to a three-electrode cell with SCE reference electrode (E= 0.241 V vs. NHE) and a Pt net as counter electrode. The measurements were conducted in Ringer solution (8 g/L NaCl, 0.2 g/L KCl, 0.2 g/L $CaCl_2$ and 1 g/L $NaHCO_3$) with pH = 7.4 at 310 K. The electrolyte was purged with N_2 for 1 h before each test. Measurements were started after 30 min of immersion in the Ringer solution under open circuit potential (OCP) conditions and the OCP potential has been recorded vs. time. The dynamic polarization was started from the cathodic regime (-1V vs. SCE) and linearly swept in the anodic direction at a rate of 0.5 mV/s up to 4V. Anodic current transient measurements were performed by implementing potential steps from the OCP to selected anodic potentials, which were chosen from the potentiodynamic polarization curves.

For cyclic voltammetric measurements the samples have been used as rotating disc electrodes implemented in an EG&G Parc Model 616 device which realized a rotation speed of 2000 rpm. After immersion of samples under open circuit potential (OCP) conditions for 30 min and holding at an initial potential of -1.5 V for 60 sec, the potential was swept up to 4 V vs. SCE at a rate of 20 mV/sec in anodic direction and then reversed in cathodic direction up to the initial potential.

Each electrochemical measurement was repeated 3-4 times to ensure a suitable level of reproducibility. Electrochemical parameters (corrosion potential, corrosion current density, passive current density) were calculated as mean values and the standard deviation from the mean values were determined.

2.3 *Surface analytical measurements*

X-ray photoelectron spectroscopy (XPS) measurements were performed to analyze the chemical composition of the surface of $Ti_{75}Zr_{10}Si_{15}$ and $Ti_{60}Zr_{10}Nb_{15}Si_{15}$ ribbons as exposed to air and also after immersion in Ringer solution for 20 hours. It has been done at a PHI 5600 CI (Physical Electronics) spectrometer using non-monochromatic Mg-Kα X-rays (350 W) for excitation. A hemispherical analyzer working at pass energy of 29 eV was applied to record the spectra. The analysis area was around 800 μm in diameter. Residual binding energy (BE) shifts from surface charging was corrected by shifting the BE values with respect to the Ti2p peak at 458.8 eV according to TiO_2 [27]. Peak fitting was performed using the PHI-MultiPak software (version 9.3, 2011).

Auger electron spectroscopy (AES) in connection with sputter depth profiling was performed to analyze the chemical composition across the passive layer of $Ti_{75}Zr_{10}Si_{15}$ and $Ti_{60}Zr_{10}Nb_{15}Si_{15}$ ribbons after different treatments and after anodic polarization at two selected potentials (see section 3.3). A JAMP 9500 F Field Emission Microprobe (JEOL) equipped with a hemispherical analyzer with electron beam conditions of 10 keV and 10 nA was used. A scanned beam of Ar^+ ions of 1 KeV with the scan size of 1 mm x 1 mm has been used which results in a determined sputtering rate of 4.7 nm/min in SiO_2. This sputtering rate has been used as a reference for measuring the thickness of oxide films. From the half width values of the oxygen concentration profiles (middle sputter time), thickness values were estimated. The difference between the sputter time before the middle value and the one after it, has been used to calculate the error bar values.

Because in such oxide and multicomponent materials oxide reduction and preferential sputtering lead to changes of the surface composition during sputter depth profiling which have to be considered. We used a semi-quantitative correction for this in the depth profiles using internal surface and bulk reference information. Because of peak shape changes this correction procedure was using the non-differentiated Auger spectra; details are described elsewhere [28].

2.4 *SBF test*

The apatite-forming ability on surfaces of $Ti_{75}Zr_{10}Si_{15}$ and $Ti_{60}Zr_{10}Nb_{15}Si_{15}$ ribbons was tested in a simulated body fluid (SBF). Its composition which was prepared according to Kokubo and Takadama [29] consisted of NaCl (7.92 g/L), $NaHCO_3$ (0.356 g/L), KCl (0.376 g/L), $Na_2HPO_4.3H_2O$ (0.147 g/L), $MgCl_2.6H_2O$ (0.309 g/L), 1M HCl (15 mL), $CaCl_2$ (0.375 g/L), Na_2SO_4 (0.162 g/L), Tris (6.12 g/L). Firstly, samples were cleaned ultrasonically in ethanol for 15 min and dried at 100°C. Then, they were treated in 10 M NaOH at 60°C for 24 hours to increase their bioactivity. Subsequently, the samples were cleaned with bi-distilled water for a short time and dried in a laminar flow box for 24 hours at room temperature [30]. At the end, they were immersed in SBF solution at 37°C for 10, 20 and 30 days and cleaned three times with bi-distilled water and then dried in a laminar flow box for 24 hours at room temperature. After this treatment, the surface of samples was investigated with SEM and energy-dispersive X-ray spectroscopy (EDX).

3. Results and discussion

3.1 Microstructure characterization

$Ti_{75}Zr_{10}Si_{15}$ and $Ti_{60}Zr_{10}Nb_{15}Si_{15}$ rods with 4 mm diameter were produced by copper mold casting. A fully crystalline structure is observed for the rod samples due to the low cooling rates (~1 K/sec). In contrast, melt-spinning with about 10^6 K/sec cooling rate yields ribbons with nanocomposite structure, i.e. with a main glassy matrix phase. Figure 1a shows XRD patterns of the crystalline rod and in the inset, those of the air- and wheel-side of melt-spun ribbons (quenched from a melt temperature of 1993K) of $Ti_{75}Zr_{10}Si_{15}$. The crystalline ternary alloy is of multiphase nature and comprises one hexagonal intermetallic phase $(Ti,Zr)_5Si_3$ (S1) and an eutectic of S1 and hexagonal α-Ti phase [25]. Conversely, XRD patterns of ribbons reveal a glassy-nanocrystalline composite structure. TEM studies confirmed a glassy matrix with some embedded nanocrystals of 5-50 nm size identified as bcc β-Ti [25]. As it can be derived from the XRD patterns, the glassy phase fraction increases from the airside of the ribbon towards the wheelside which is explained by the cooling rate gradient during single-roller melt-spinning.

Figure 1b shows XRD patterns of the crystalline rod and of the air- and wheel-side of glassy ribbons (quenched from 1993K) of $Ti_{60}Zr_{10}Nb_{15}Si_{15}$. The crystalline alloy is similarly to the ternary one, of multiphase nature and consists of Nb-stabilized phases, i.e. the S1 phase $(Ti,Zr,Nb)_5Si_3$ and an eutectic of S1 and bcc β-Ti(Nb) phase. Upon melt-spinning the Nb addition caused an increase of the glass-forming ability (implying a reduction of the fraction of β-Ti(Nb) nanocrystals). Similarly to the ternary alloy, there is a slight cooling rate gradient over the ribbon cross-section that causes a certain reduction of the fraction of β-Ti(Nb) nanocrystals to a nearly fully glassy state towards the wheel side (all details in [25]).

For the corrosion studies, we chose melt-spun alloy samples with the maximum achievable microstructural homogenization state, i.e. maximum glassy phase fraction in the respective alloy system. Both, the glass-matrix and the nanocrystals are of Ti-base (with different concentrations of other alloy constituents as solute species). Thus, chemical fluctuations at the nanoscale may not be significant for the corrosion behavior. Due to the fragility of the thin ribbons, separate preparation of ribbon sides for electrochemical studies was not possible. Though being aware of the morphological (roughness) and slight microstructural differences between ribbon sides, we considered those alloy samples as "nearly homogeneous and mainly glassy states" in comparison to the heterogeneous multiphase micro-crystalline states of the cast alloy counterparts and to the polycrystalline states of the single constituents and of β-type Ti-40Nb used as reference materials.

3.2 Potentiodynamic polarization behavior in Ringer solution

For acquiring qualitative information about principal anodic oxidation reactions, cyclic voltammetric measurements (CVs) were conducted. In Fig. 2, CVs for $Ti_{75}Zr_{10}Si_{15}$ and $Ti_{60}Zr_{10}Nb_{15}Si_{15}$, for the metallic constituents and for Ti-40Nb are shown. All measurements were carried out in Ringer solution at 37°C with a scan rate of 20 mV/sec. After OCP adjustment, the samples were firstly polarized up to -1.5 V vs. SCE and this potential was kept constant for 60 sec for pre-reduction of the electrode surface. Then, potential scanning up to 4 V vs. SCE and backwards was started. In Fig. 2 mainly the anodic parts of the CVs are shown.

CVs for Ti, Zr, Nb and Ti-40Nb are summarized in Fig. 2a and are interpreted based on literature sources [30-37]. The OCP values for Ti and Nb adjust at -0.025±0.025 V vs. SCE and -0.275±0.025 V vs. SCE, respectively. In the CVs, Ti and Nb show a typical valve-metal

behavior in a wide potential range, i.e. a very low anodic reactivity due to formation of barrier-type passive films and no pitting [33]. The anodic response of Ti is indicative for the initial formation of Ti^{3+}-species as films of TiOOH and Ti_2O_3 and the subsequent transformation into Ti^{4+}- species corresponding to TiO_2 starting at potentials of 0.4V vs. SCE. The anodic behavior of Nb is initially governed by the formation of NbO (Nb^{2+}) and NbO_2 (Nb^{4+}) oxides which further partially transform to Nb_2O_5 (Nb^{5+}). Unlike Ti and Nb, Zr shows in Ringer solution a limited corrosion resistance. The OCP value establishes at -0.195±0.025 V vs. SCE and after pre-reduction only a short region of anodic passivity is observed before it undergoes active dissolution at around 0.2 V vs. SCE with a sudden increase of the current density. This behavior is indicative for pitting. The CV of Ti-40Nb is quite similar to that of Ti and Nb in the measured potential range. The anodic step starting at ~1.2 V vs. SCE is attributed to limited oxygen evolution from water-decomposition. Metikos-Hukovic et al. [30] stated that addition of Nb to a Ti alloy instead of V leading to (α+β) Ti6Al6Nb improved markedly the passive film stability. The beneficial effect of Nb is attributed to an annihilation of anion vacancies in the crystal lattice of the TiO_2 passive film, which occur due to the presence of lower oxidation states (Ti^{2+}, Ti^{3+}). Thus, Nb makes the passive oxide film more stoichiometric. However, in the anodic section of the CV for Ti-40Nb at potentials >1.2 V vs. SCE a higher current density level than for the single constituents is measured. This may be attributed to a stronger distortion of the structure of the rapidly growing passive film on the alloy, which enables an enhanced transfer or tunneling of electrons which is needed for the water decomposition reaction.

Fig. 2b shows the CVs of $Ti_{75}Zr_{10}Si_{15}$ and $Ti_{60}Zr_{10}Nb_{15}Si_{15}$ prepared as multiphase micro-crystalline cast rods and as homogenized melt-spun ribbons with nearly fully glassy state.

The overall electrochemical behavior of all the alloy samples is similar to that of pure Ti and Nb as well as of β-Ti-40Nb in the potential range up to ~1.2 V, i.e. a spontaneous stable passivation due to barrier-type oxide film formation. In detail, an initial slight increase of anodic current densities due to sub-oxide formation occurs at anodic potentials of ~-0.6 V vs. SCE. Further slight increases of current density values are ascribed to oxide transformations to higher valence states and thickening of the oxide film up to the potential of the water stability limit [30]. The additionally observed small peaks for a $Ti_{75}Zr_{10}Si_{15}$ ribbon at ~0.1 V vs. SCE, which are at the same potential range as the initial pitting potential of Zr, can be attributed to temporary pitting initiation due to the Zr fraction in the alloy.

In order to experimentally check the proposed oxide film formation, surface analysis of $Ti_{75}Zr_{10}Si_{15}$ and $Ti_{60}Zr_{10}Nb_{15}Si_{15}$ melt-spun ribbon samples has been done by means of XPS. It was performed on the air-side of polished ribbons samples which were exposed to air for 24 hours and for samples that were immersed in Ringer solution (37°C) at OCP condition for 20 hours after polishing. Upon this pre-treatment similar surface reactions can be expected as those taking place upon fast potentiodynamic polarization of freshly polished and pre-reduced samples. The high resolution spectra of all alloying elements and of oxygen are exemplarily shown for air-exposed states for $Ti_{60}Zr_{10}Nb_{15}Si_{15}$ ribbons in Fig. 3a. Several literature sources have been used for indexing the peaks of all observed chemical states [27,38-40]. According to this, peak fits for the appropriate components were perfomed and are presented in Fig. 3a. For both alloys, peaks of all alloying elements in the metal states (Me^{o}) are present which reveals that the spontaneously formed passive films are very thin. In the spectra of Ti 2p three doublets are observed corresponding to Ti^{2+}, $Ti^{3+}$and Ti^{4+} with main presence of Ti^{4+} peaks [6,41]. For Zr 3d, a doublet of $3d_{5/2}$ and $3d_{3/2}$ peaks from the Zr^{4+}

state is identified at 182.5 and 184.8 eV, besides detectable Zr^0 peaks. The binding energy of Si 2p at 102 eV exhibits the presence of the Si^{4+} state and the peak at 98 eV is demonstrating Si^0. In case of $Ti_{60}Zr_{10}Nb_{15}Si_{15}$, in addition, for Nb 3d multiple valence states are detected. The dominating doublet at 207.3 eV and 210 eV is ascribed to the Nb^{5+} main state while beside some residuals of the Nb^0 state (202.2 eV and 205.1 eV) weaker peaks at 203.5 and 206 eV can be related to sub-oxides with states of Nb^{4+} (NbO_2) or Nb^{2+} (NbO). All O 1s spectra comprise a main peak of the O^{2-} state at 530.5 eV. Therefore, it can be concluded that the passive film on the ternary alloy is mainly composed of TiO_2, ZrO_2, SiO_2 and that on the quaternary alloy comprises in addition Nb_2O_5. Also, formation of mixed oxides of the constituents may be considered. Besides that the O 1s spectra comprise two lower peaks at 532.0 and 533.5 eV which are attributed to oxygen states in OH^- and adsorbed H_2O.

A direct comparison of the detailed spectra measured for air-exposed samples and for samples immersed in Ringer solution for $Ti_{60}Zr_{10}Nb_{15}Si_{15}$ melt-spun ribbons is shown in Fig. 3b. It reveals for all alloying elements a decrease of the peak intensities of the lower valence oxide states and of the metallic state after immersion in Ringer solution. This is the consequence of an accelerated passive film growth in the aqueous medium based on the formation of oxides corresponding to the higher valence states of the alloy constituents. An increase of the OH^- and H_2O shoulders in the O 1s spectrum for the Ringer immersed samples is consistent with the raise of hydroxides and adsorbed H_2O on the surface of sample after immersion in an aqueous medium. It can be concluded that on both alloy surfaces, all alloying elements in both systems contribute to the passive film growth in air and in Ringer solution under OCP condition. These natural passive films comprise mainly higher valence

oxides, but there is also some evidence for residuals with lower valence oxide states of Ti and Nb.

In the cyclic voltammetric curve of the crystalline $Ti_{60}Zr_{10}Nb_{15}Si_{15}$ alloy in Figure 2b a small peak of the current density at about 1.5 V vs. SCE occurs because of limited temporary electron-transfer for the water decomposition. But when further increasing the potential, the current density establishes at another low plateau indicating a further stable film growth [30]. Under the conditions of a CV, the anodic behavior of the multiphase $Ti_{60}Zr_{10}Nb_{15}Si_{15}$ alloy is very similar to that of the single-phase β-type Ti-40Nb reference alloy (with 25.6 at.-% Nb). Melt-spun ribbons of $Ti_{60}Zr_{10}Nb_{15}Si_{15}$ show a similar anodic behavior like the ternary alloy but a lower overall current density level, indicating enhanced corrosion protection. As it has been discussed before, addition of Nb to a Ti alloy can improve the corrosion stability.

Further characteristic features in the anodic regimes of the CVs of the melt-spun ribbons in Figure 2b are sharp peaks at ~1.6 V vs. SCE and subsequent smaller peaks at ~2 V vs. SCE. In the measurements on the cross sections of the crystalline counterpart rods these peaks are not so pronounced. They are attributed to a possible beginning electron-transfer reaction that enables water decomposition under oxygen evolution which is upon further polarization inhibited by enhanced oxide growth. Also, upon measurements on ribbon samples, current density fluctuations are observed at potentials above 3 V vs. SCE which suggest a metastable breakdown of passivity. It is reasonable to assume that these features are artifacts that must be attributed to the samples geometry with sharp edges.

Quasistatic linear polarization curves were recorded in Ringer solution at 37 °C (Fig. 4). For the different materials tested in this study, we selected one representative curve after

several repeated measurements. All investigated Ti-based systems show spontaneous passivity even in a highly concentrated chloride solution (Ringer solution) at near neutral pH value (7.4). This low reactivity makes free corrosion and anodic conditions corresponding to an overall very low current density level. At this level, fluctuations of the curves observed in repeated measurements must be mainly attributed to (manual) sample handling prior to the electrochemical measurements. Cp-Ti and single-phase β-Ti-40Nb have been selected as references. For cp-Ti, the free corrosion potential established at about -0.250±0.025 V vs. SCE and a rather low corrosion current density of only 45±5 nA/cm^2 is observed. This transfers into a spontaneous passivation of the surface in the anodic potential regime corresponding to a plateau-like behavior at a current density level of 3.5±0.5 µA/cm^2 below 1 V vs. SCE. A very similar behavior is observed for Ti-40Nb; it exhibits a very low corrosion current density of 4±4 nA/cm^2 and transfers spontaneously to a stable passive regime at a current density level of 2.5±0.5 µA/cm^2 up to 1 V vs. SCE.

The anodic polarization curves for $Ti_{75}Zr_{10}Si_{15}$ and $Ti_{60}Zr_{10}Nb_{15}Si_{15}$ rods and ribbons are shown in Figure 4. In case of the crystalline alloy states, similar as for Ti-40Nb, adding alloying elements (Zr, Si, Nb) to Ti shifts the corrosion potential to more negative values (to -0.350±0.025 V vs. SCE for the ternary alloy and to -0.460±0.025 V vs. SCE for the quaternary alloy) and slightly lowers the corrosion rate corresponding to slight reduction of the corrosion current density to 40±5 nA/cm². Upon anodic polarization up to ~1.2 V vs. SCE, both crystalline alloys spontaneously passivate. The passive current densities are of comparable level as for cp-Ti and Ti-40Nb, i.e. in the range of 2±1 µA/cm². For both multiphase alloys, there is no passive layer breakdown in this potential range. Moreover,

beyond the water stability potential range both alloys remain passive up to about 3 V vs. SCE, above which some metastable pitting is possible (current fluctuations).

Homogenization of the microstructural state of Ti-Zr-(Nb)-Si alloys by melt-spinning does not significantly change the polarization behavior under quasistatic conditions. The corrosion potentials are slightly shifted to more positive values by about 200 mV, but the corrosion current density remains at a similar very low level of 40±5 nA/cm². Upon anodic polarization, surface passivation is enhanced and a passive current density level similar to that measured for the crystalline counterparts is maintained in the potential range of water stability. For both nearly fully glassy alloys, pitting was not observed upon further polarization (>1.2 V vs. SCE). Some typical features, "water decomposition peaks", occur which must be ascribed to the problematic geometry of the ribbon samples that was discussed before.

Similar as for cp-Ti, the melt-spun ternary alloy exhibits a gradual increase of the current during the high polarization regime. This is an indication for a certain electron-permeability of the growing oxide film, which is for Ti known to be due to the semi-conductive properties of the film. The melt-spun $Ti_{60}Zr_{10}Nb_{15}Si_{15}$ alloy shows stable passivity in this high polarization regime with some weak indication for metastable pitting at >3 V vs. SCE.

Similar investigations have been done by Qin et al. for glass-forming Ti-Zr-Cu-Pd-Sn alloys and by Oak et al. for Ti-Zr-Ta-Si alloys in body simulated fluids at 37 °C. They conducted quasistatic polarization measurements up to 1.5 V vs. SCE [9,10,42,43]. For Cu-containing alloys certain passivity break downs and pitting events occur at defined potentials less than 1.5 V vs. SCE, but Ti-Zr-Ta-Si alloy systems demonstrate a similar stable behavior

as that of our alloys up to 1.5 V vs. SCE. In comparison, in the present study we proved for melt-spun $Ti_{75}Zr_{10}Si_{15}$ and $Ti_{60}Zr_{10}Nb_{15}Si_{15}$, a very high stability of the passive state in a wider anodic potential range, i.e. even beyond the water stability limit.

3.3 Passivity and pitting under potentiostatic control

In order to study the anodic passive film growth mechanism in more detail, anodic current density transients were recorded for $Ti_{75}Zr_{10}Si_{15}$ and $Ti_{60}Zr_{10}Nb_{15}Si_{15}$ melt-spun ribbons which are shown in the double-logarithmic plot in Fig. 5. Measurements have been carried by stepping the potential from a stable OCP to two different anodic potentials, one in the range of the stable passive region, i.e. at 0.5 V vs. SCE, and another one in the high polarization regime, i.e. at 4 V vs. SCE. As reference material the single-phase Ti-40Nb was employed here, as it exhibits very precisely the characteristic anodic behavior of valve-metals [6].

In the case of Ti-40Nb when stepping the potential to 0.5 V vs. SCE, the measurable current density transient is after an initial period clearly linear with a slope close to m= -1. This is indicative for a high-field-controlled passive film growth [33]. When stepping the potential to a higher value of 4 V vs. SCE, a similar linear behavior at a higher current density level is observed. This demonstrates the rapid formation of a barrier-type passive film with no or very low permeability for electric charges (electrons) even at this extreme polarization condition.

Compared to this nearly ideal behavior of Ti-40Nb, for both melt-spun Ti-(Nb)-Zr-Si alloys the current transients obtained when stepping the potential to 0.5V vs. SCE are very similar.

This confirms that also for these nearly fully glassy alloy samples the high-field growth mechanism holds. There is no significant difference between ternary and quaternary alloy.

In contrast, when stepping the potential to the high polarization regime (4 V vs. SCE) a deviation from the ideal behavior occurs for both glassy alloys. In repeated measurements, for the melt-spun $Ti_{75}Zr_{10}Si_{15}$ alloy current density transients were measured at rather high levels with a mean slope m~0. Those are characteristic for metal dissolution which will in this case superimpose the limited water decomposition reaction (that was detected in quasistatic polarization experiments). Additional SEM analysis of ribbon samples after the transient measurements (Fig. 6) revealed local corrosion damages which were initiated at various defect sites of a ribbon surface. The images clearly show a quite uniform propagation of the corrosion front leading to a nearly spherical damage. This confirms a monotonic rate of the corrosion reaction in the metastable nearly single-phase glassy material. Current transients recorded for melt-spun $Ti_{60}Zr_{10}Nb_{15}Si_{15}$ samples comprise an initial period of dominant corrosion followed by a transfer into stable passive film growth similar as observed for Ti-40Nb. After detecting metastable pitting at this high potential regime under quasistatic polarization conditions (Fig. 4), this indicates that under potential-stepping conditions the Nb-containing glassy alloy has a certain tendency for healing its surface after a corrosion initiation event.

For further detailed characterization of the passive films that form on the glass-forming Ti(-Nb)-Zr-Si alloys in simulated body fluids under potentiostatic control, sputter depth-profiling was conducted. The AES method was identified as being the favored method in comparison with XPS for this purpose because of higher sputtering rates and well defined measuring area selection [28].

Sample surfaces were immersed in Ringer solution under OCP condition and were also anodically polarized at 0.5 V and 4 V vs. SCE before analysis. Fig. 7 summarizes exemplary depth profiles obtained by AES sputter depth profiling of $Ti_{60}Zr_{10}Nb_{15}Si_{15}$ sample surfaces. The AES profile of the surface region of a naturally passivated reference sample (Fig. 7a) reveals that the oxygen concentration gradually decreases within the first ~100 seconds of sputter time which corresponds to an oxide thickness of below 10 nm.

Correspondingly, the concentrations of the alloying element species Ti, Zr, Nb and Si gradually increase up to a plateau level. This plateau is indicative for the surface region of the metallic state with the nominal concentration of the alloying elements. The initial sputter time period at which the elemental concentrations including O gradually decay is the passive film region. More strictly, the sputter time at which the oxygen signal decayed to the half width value between maximum and minimum value was defined as oxide/metal interface.

AES analysis confirms that all constituent element species are present in the oxide film, whereby the Ti oxide species fraction dominates. The depth profiles of samples immersed in Ringer solution under OCP conditions and polarized at 0.5 V vs. SCE (Fig.7b, c) are very similar showing only a gradual expansion of the surface oxide region. Polarization at 4 V vs. SCE (Fig. 7d) strongly enhances the passive film growth. The oxygen concentration remains at a plateau level within the first ~400 sec of sputtering and only then steeply decreases reflecting the oxide/metal interface region. Accordingly, the Ti concentration decayed only marginally in the oxide layer region with a slight trend to deplete towards the inner interface. From the concentration profiles of the other constituent elements a two-zone nature of the passive film can be derived. In the outermost zone (<200 sec sputter time) Si species are

strongly depleted (close to 0%) relative to Zr and Nb species, whereby Si is relatively enriched in the inner oxide film zone (~200-400 sec).

From the half width values of the oxygen concentration profiles thickness values of the passive films were estimated considering a reference sputter time of the AES system in SiO_2 of 4.7 nm/min. Results of this estimation for both alloys are summarized in Figure 8. It is evident that addition of Nb to the nearly fully glassy $Ti_{75}Zr_{10}Si_{15}$ alloy does not significantly change the passive film thickness. Immersion in Ringer solution or anodization at 0.5 V vs. SCE leads to a slight increase of the film thickness, but values remain small, i.e. <10 nm. Polarization at 4 V vs. SCE results in a marked thickness rise by about 5 times to 35±2 nm.

3.3 Apatite-forming ability

The analysis of hydroxyapatite formation on a material in a SBF solution may be used as a preliminary assessment of the in vivo bone bioactivity of that material [29]. Therefore, the ability of the melt-spun $Ti_{75}Zr_{10}Si_{15}$ and $Ti_{60}Zr_{10}Nb_{15}Si_{15}$ alloys to generate hydroxyapatite at their surface (airsides) was tested and compared against that of cp-Ti. Samples of those three materials were immersed in SBF solution for 10, 20 and 30 days. Subsequently, their surface was investigated by SEM and EDX. Selected SEM images are shown in Fig. 9. Highly porous layers developed by overlapping of hemispherical growth centres. EDX analysis (spectra not shown here) revealed the presence of both Ca and P in those layers indicating that they consist of hydroxyapatite. The growth of the hydroxyapatite layer appears to occur at similar rates on cp-Ti and on the melt-spun $Ti_{75}Zr_{10}Si_{15}$ alloy: after 10 days they show a similar morphology of the hydroxyapatite layer (see Fig. 9a and b). However, the growth rate on the $Ti_{60}Zr_{10}Nb_{15}Si_{15}$ alloy is significantly lower. As Fig. 9c shows, after 10 days of

exposure to the SBF solution, only few small porous growth centres were detected (this is similar after 20 days). Nevertheless, after 30 days (see Fig. 9d) the $Ti_{60}Zr_{10}Nb_{15}Si_{15}$ alloy also forms a thick layer of hydroxyapatite.

It is concluded that the melt-spun $Ti_{75}Zr_{10}Si_{15}$ alloy has an apatite-forming ability which is similar to that of cp-Ti. For the melt-spun $Ti_{60}Zr_{10}Nb_{15}Si_{15}$ alloy, the formation of hydroxyapatite is retarded, suggesting that additions of Nb inhibit the apatite-forming ability of Ti-based alloys. This is in agreement with previous studies on β-phase alloys which also revealed a reduced rate of the apatite-forming ability when adding 45 wt.-% Nb to pure Ti [7].

3. Conclusions

In the present study the corrosion and passivation behavior of glass-forming $Ti_{75}Zr_{10}Si_{15}$ and $Ti_{60}Zr_{10}Nb_{15}Si_{15}$ alloys in simulated body fluid (Ringer solution) at 310 K was assessed. Both alloys show in the multiphase crystalline state as well as in the homogenized mainly glassy state very low corrosion rates which are comparable to those of cp-Ti or β-phase Ti-40Nb. Upon anodic polarization, formation of barrier-type protective passive films under participation of all alloy constituents dominates. Zr must be considered as critical element that can induce pitting. But homogeneous constituent distribution in the melt-spun mainly glassy state and substitution of Ti with Nb fractions in the alloy composition can counteract its effect. Altogether, their anodic stability is superior to that of Cu-containing glass-forming Ti alloys and is comparable to that of glassy Ti-Zr-Ta-Si alloys and of β-type Ti-40Nb. SBF testing proved an apatite-forming ability of the mainly glassy alloy surfaces which is

comparable to that of cp-Ti for the ternary alloy, but is somewhat retarded when Nb is added to the alloy.

In conclusion, glass-forming $Ti_{75}Zr_{10}Si_{15}$ and $Ti_{60}Zr_{10}Nb_{15}Si_{15}$ alloys which are free of toxic elements appear to be very good candidates for long-term biomedical applications due to the proven high stability of their passive states in a simulated body fluid. The addition of Nb supports a high pitting resistance even under extreme anodic polarization conditions. The Nb-containing nearly single-phase glassy alloy has similar corrosion properties to the single-phase β-type Ti-40Nb alloy. The limited glassy sample thickness <1 mm related with the limited glass-forming ability suggests the new alloys as excellent coating materials for medical devices with high wear and corrosion resistance.

Acknowledgements

The authors thank S. Donath for preparing samples, M. Johne for electrochemical measurements and S. Kaschube for AES measurements. Funding by the European Commission within the framework of the FP7-ITN network BioTiNet (PITN-GA-2010-264635) and by the DFG within the SFB-Transregio 79, project M1 is gratefully acknowledged. Partial funding from the MAT2011-27380-C02-01 from the Spanish MINECO is also acknowledged.

References

[1] Geetha M, Singh AK, Asokamani R, Gogia AK. Ti based biomaterials, the ultimate choice for orthopaedic implants – A review. Prog Mater Sci 2009;54:397-425.

[2] Balamurugan A, Rajeswari S, Balossier G, Rebelo AHS, Ferreira JMF. Corrosion aspects of metallic implants - An overview. Mater Corros 2008;59:855-69.

[3] Lin CH, Huang CH, Chuang JF, Huang JC, Jang JS, Chen CH. Rapid screening of potential metallic glasses for biomedical applications. Mater Sci Eng C-Mater Biol Appl 2013;33:4520-6.

[4] Niinomi M. Recent research and development in titanium alloys for biomedical applications and healthcare goods. Sci Technol Adv Mat 2003;4:445-54.

[5] Hanada S, Matsumoto H, Watanabe S. Mechanical compatibility of titanium implants in hard tissues. Int Congr Ser 2005;1284:239-47.

[6] Helth A, Gostin PF, Oswald S, Wendrock H, Wolff U, Hempel U, et al. Chemical nanoroughening of Ti40Nb surfaces and its effect on human mesenchymal stromal cell response. J Biomed Mater Res B 2014;102(1):31-41.

[7] Gostin PF, Helth A, Voss A, Sueptitz R, Calin M, Eckert J, et al. Surface treatment, corrosion behavior, and apatite-forming ability of Ti-45Nb implant alloy. J Biomed Mater Res B 2013;101B:269-78.

[8] Oak JJ, Louzguine-Luzgin DV, Inoue A. Investigation of glass-forming ability, deformation and corrosion behavior of Ni-free Ti-based BMG alloys designed for application as dental implants. Mater Sci Eng C-Mater Biol Appl 2009;29:322-7.

[9] Oak JJ, Louzguine-Luzgin DV, Inoue A. Fabrication of Ni-free Ti-based bulk-metallic glassy alloy having potential for application as biomaterial, and investigation of its mechanical properties, corrosion, and crystallization behavior. J Mater Res 2007;22:1346-53.

[10] Qin F, Wang X, Zhu S, Kawashima A, Asami K, Inoue A. Fabrication and Corrosion Property of Novel Ti-Based Bulk Glassy Alloys without Ni. Mater Trans 2007;48:515-8.

[11] Morrison ML, Buchanan RA, Peker A, Liaw PK, Horton JA. Electrochemical behavior of a Ti-based bulk metallic glass. J Non-cryst Solids 2007;353:2115-24.

[12] Zhu SL, Wang XM, Qin FX, Inoue A. A new Ti-based bulk glassy alloy with potential for biomedical application. Mat Sci Eng A-Struct 2007;459:233-7.

[13] Oak J-J, Inoue A. Formation, mechanical properties and corrosion resistance of Ti–Pd base glassy alloys. J Non-cryst Solids 2008;354:1828-32.

[14] Xie GQ, Qin FX, Zhu SL. Recent Progress in Ti-Based Metallic Glasses for Application as Biomaterials. Mater Trans 2013;54:1314-23.

[15] Gu XJ, Poon SJ, Shiflet GJ, Lewandowski JJ. Compressive plasticity and toughness of a Ti-based bulk metallic glass. Acta Mater 2010;58:1708-20.

[16] Calin M, Gebert A, Ghinea AC, Gostin PF, Abdi S, Mickel C, et al. Designing biocompatible Ti-based metallic glasses for implant applications. Mater Sci Eng C-Mater Biol Appl 2013;33:875-83.

[17] Elshahawy WM, Watanabe I, Kramer P. In vitro cytotoxicity evaluation of elemental ions released from different prosthodontic materials. Dent Mater 2009;25:1551-5.

[18] Okazaki Y, Gotoh E. Comparison of metal release from various metallic biomaterials in vitro. Biomaterials 2005;26:11-21.

[19] Atapour M, Pilchak AL, Frankel GS, Williams JC. Corrosion behavior of beta titanium alloys for biomedical applications. Mater Sci Eng C-Mater Biol Appl 2011;31:885-91.

[20] Yang S, Zhang DC, Wei M, Su HX, Wu W, Lin JG. Effects of the Zr and Mo contents on the electrochemical corrosion behavior of Ti22Nb alloy. Mater Corros 2013;64:402-7.

[21] Wang BL, Zheng YF, Zhao LC. Effects of Hf content and immersion time on electrochemical behavior of biomedical Ti-22Nb-xHf alloys in 0.9% NaCl solution. Mater Corros 2009;60:330-5.

[22] Gebert A, Gostin PF, Uhlemann M, Eckert J, Schultz L. Interactions between mechanically generated defects and corrosion phenomena of Zr-based bulk metallic glasses. Acta Mater 2012;60:2300-9.

[23] Gebert A, Gostin PF, Schultz L. Effect of surface finishing of a Zr-based bulk metallic glass on its corrosion behaviour. Corros Sci 2010;52:1711-20.

[24] Oak JJ, Kimura H, Inoue A. Effects of Additional Elements on Structure, Mechanical Strength and Chemical Properties of Ni-Free Ti-Based Bulk Metallic Glasses for Biomaterials. Adv Mat Res 2007;26-28:785-8.

[25] Abdi S, Khoshkhoo MS, Shuleshova O, Bönisch M, Calin M, Schultz L, et al. Effect of Nb addition on microstructure evolution and nanomechanical properties of a glass-forming Ti–Zr–Si alloy. Intermetallics 2014;46:156-63.

[26] Scully JR, Gebert A, Payer JH. Corrosion and related mechanical properties of bulk metallic glasses. J Mat Res 2007;22:302-13.

[27] Moulder J, Stickle W, Sobol P. Handbook of X Ray Photoelectron Spectroscopy (P/N 624755): Perkin-Elmer, Physical Electronics Division; 1993.

[28] Oswald S, Gostin PF, Helth A, Abdi S, Giebeler L, Wendrock H, et al. XPS and AES sputter-depth profiling at surfaces of biocompatible passivated Ti-based alloys: Concentration quantification considering chemical effects. Surface Interface Anal accepted.

[29] Kokubo T, Takadama H. How useful is SBF in predicting in vivo bone bioactivity? Biomaterials 2006;27:2907-15.

[30] Metikoš-Huković M, Kwokal A, Piljac J. The influence of niobium and vanadium on passivity of titanium-based implants in physiological solution. Biomaterials 2003;24:3765-75.

[31] Pankuch M, Bell R, Melendres CA. Composition and structure of the anodic films on titanium in aqueous solutions. Electrochim Acta 1993;38:2777-9.

[32] Harrison JA, Williams DE. A note on the passive active transition of titanium in sulfuric-acid. Electrochim Acta 1982;27:891-5.

[33] Lohrengel MM. Thin anodic oxide layers on aluminum and other valve metals - high-field regime. Mater Sci Eng R-Rep 1993;11:243-94.

[34] Heusler KE, Schulze M. Electron-transfer reactions at semiconducting anodic niobium oxide films. Electrochim Acta 1975;20:237-44.

[35] Freitas MBJG, Bulhoes LOS. Breakdown and crystallization processes in niobium oxide films in oxalic acid solution. J Appl Electrochem 1997;27:612-5.

[36] Oliveira NT, Biaggio SR, Rocha-Filho RC, Bocchi N. Electrochemical studies on zirconium and its biocompatible alloys Ti-50Zr at.% and Zr-2.5Nb wt.% in simulated physiologic media. J Biomed Mater Res Part A 2005;74:397-407.

[37] Pourbaix M. Atlas of Electrochemical Equilibria in Aqueous Solutions. Oxford: Pergamon Press; 1966.

[38] Sittig C, Textor M, Spencer ND, Wieland M, Vallotton PH. Surface characterization of implant materials c.p. Ti, Ti-6Al-7Nb and Ti-6Al-4V with different pretreatments. J Mater Sci-Mater M 1999;10:35-46.

[39] Milošev I, Kosec T, Strehblow HH. XPS and EIS study of the passive film formed on orthopaedic Ti–6Al–7Nb alloy in Hank's physiological solution. Electrochim Acta 2008;53:3547-58.

[40] Atuchin VV, Kalabin IE, Kesler VG, Pervukhina NV. Nb 3d and O 1s core levels and chemical bonding in niobates. J Electron Spectrosc 2005;142:129-34.

[41] Tsutsumi Y, Nishimura D, Doi H, Nomura N, Hanawa T. Difference in surface reactions between titanium and zirconium in Hanks' solution to elucidate mechanism of calcium phosphate formation on titanium using XPS and cathodic polarization. Mater Sci Eng C-Mater Biol Appl 2009;29:1702-8.

[42] Oak JJ, Inoue A. Attempt to develop Ti-based amorphous alloys for biomaterials. Mat Sci Eng A-Struct 2007;449–451:220-4.

[43] Qin FX, Wang XM, Xie GQ, Zhu SL, Kawashima A, Asami K, et al. Microstructure and corrosion resistance of Ti-Zr-Cu-Pd-Sn glassy and nanocrystalline alloys. Mater Trans 2007;48:167-70.

Figure Captions

Figure 1 XRD patterns of a) a cast $Ti_{75}Zr_{10}Si_{15}$ rod and inset: of a melt-spun ribbon quenched from a melt temperature of 1993K (both air-side and wheel-side);

b) a cast $Ti_{60}Zr_{10}Nb_{15}Si_{15}$ rod and inset: of a melt-spun ribbon quenched from a melt temperature of 1993K (both air-side and wheel-side).

Figure 2 Anodic sections of cyclic voltammograms of a) Ti, Zr and Nb and β-type Ti-40Nb ($Ti_{74.4}Nb_{25.6}$) and b) of $Ti_{75}Zr_{10}Si_{15}$ rod, $Ti_{60}Zr_{10}Nb_{15}Si_{15}$ rod, $Ti_{75}Zr_{10}Si_{15}$ ribbon and $Ti_{60}Zr_{10}Nb_{15}Si_{15}$ ribbon, recorded in Ringer solution (pH 7.4, T= 37°C), at $\nu = 20 mV sec^{-1}$ and $\omega = 2000\ min^{-1}$.

Figure 3 a) XPS analysis of $Ti_{60}Zr_{10}Nb_{15}Si_{15}$ ribbon surface exposed to air; measured and fitted core level spectra of Ti 2p, Zr 3d, Nb 3d, Si 2p and O 1s

b) comparison of XPS analysis of $Ti_{60}Zr_{10}Nb_{15}Si_{15}$ ribbon surfaces exposed to air and immersed in Ringer solution under OCP condition for 20 hours; measured core level spectra of Ti 2p, Zr 3d, Nb 3d, Si 2p and O 1s

Figure 4 Potentiodynamic anodic polarization curves of cp-Ti, β-type Ti-40Nb ($Ti_{74.4}Nb_{25.6}$), $Ti_{75}Zr_{10}Si_{15}$, $Ti_{60}Zr_{10}Nb_{15}Si_{15}$ cast rods and of $Ti_{75}Zr_{10}Si_{15}$, $Ti_{60}Zr_{10}Nb_{15}Si_{15}$ melt-spun ribbons recorded in Ringer solution at 37°C; inset: higher resolved curve sections close to the free corrosion potential

Figure 5 Current density transients recorded upon potentiostatic anodic polarization of the β-type Ti-40Nb and $Ti_{75}Zr_{10}Si_{15}$ and $Ti_{60}Zr_{10}Nb_{15}Si_{15}$ ribbons in Ringer Solution at 37°C at selected potentials: 0.5V and 4V vs. SCE.

Figure 6 SEM images of corroded areas of a $Ti_{75}Zr_{10}Si_{15}$ ribbon sample observed after potentiostatic polarization at 4V vs. SCE in Ringer solution, a) corrosion

damage-overview, b, c) rim regions of the corrosion damage showing the front of corrosion propagation

Figure 7 Elemental concentration depth profiles obtained from AES measurements at surfaces (airside) of $Ti_{60}Zr_{10}Nb_{15}Si_{15}$ ribbons a) naturally passivated in air, b) immersed in Ringer solution at 37°C for 20 hours under OCP condition, c) after potentiostatic polarization at 0.5 V vs. SCE for 2 hours, d) after potentiostatic polarization at 4 V vs. SCE for 2 hours

Figure 8 Thickness data of the passive films formed on melt-spun of $Ti_{75}Zr_{10}Si_{15}$ and $Ti_{60}Zr_{10}Nb_{15}Si_{15}$ ribbons surfaces after I) exposure to air for 20 hours, II) immersion in Ringer solution at 37°C for 20hours, III) after anodic polarization at 0.5 V vs. SCE for 2hours, IV) after anodic polarization at 4 V vs. SCE for 2 hours. Data were obtained from AES depth profiles (Fig. 7), i.e. from analysis of the oxygen concentration change

Figure 9 SEM images of cp-Ti, $Ti_{75}Zr_{10}Si_{15}$ and $Ti_{60}Zr_{10}Nb_{15}Si_{15}$ treated with NaOH and immersed in SBF solution for different durations: (a) cpTi /10 days, (b) $Ti_{75}Zr_{10}Si_{15}$ /10 days, (c) $Ti_{60}Zr_{10}Nb_{15}Si_{15}$ /10 days, and (d) $Ti_{60}Zr_{10}Nb_{15}Si_{15}$ / 30 days.

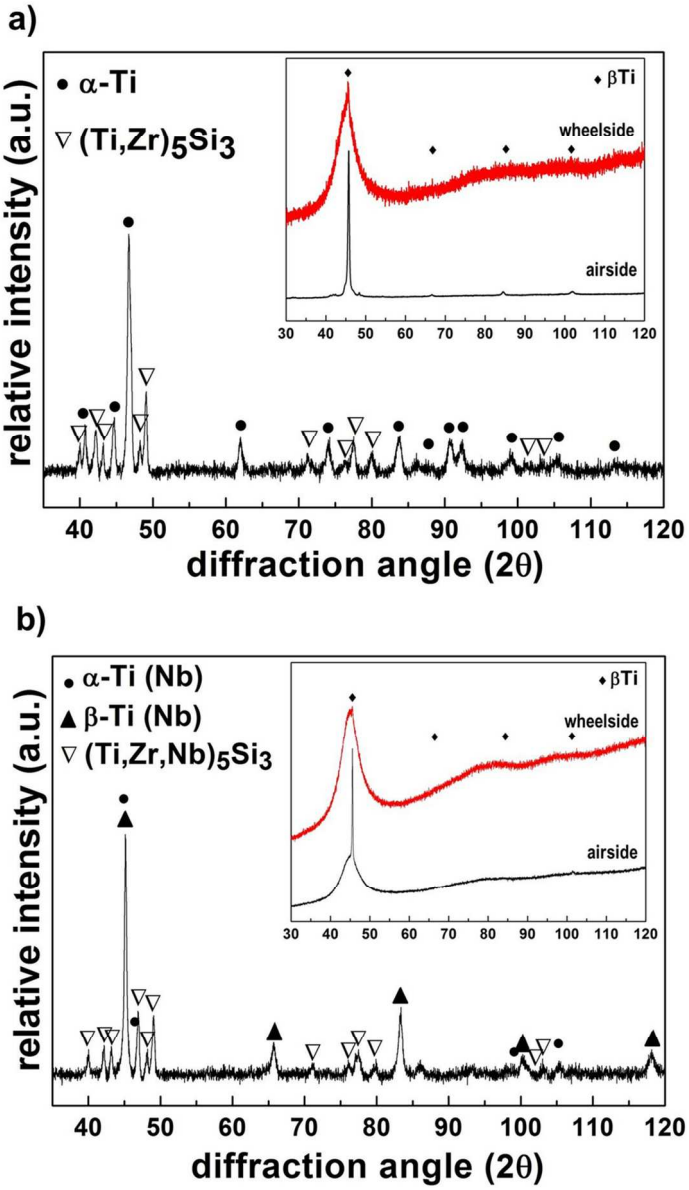

82x142mm (300 x 300 DPI)

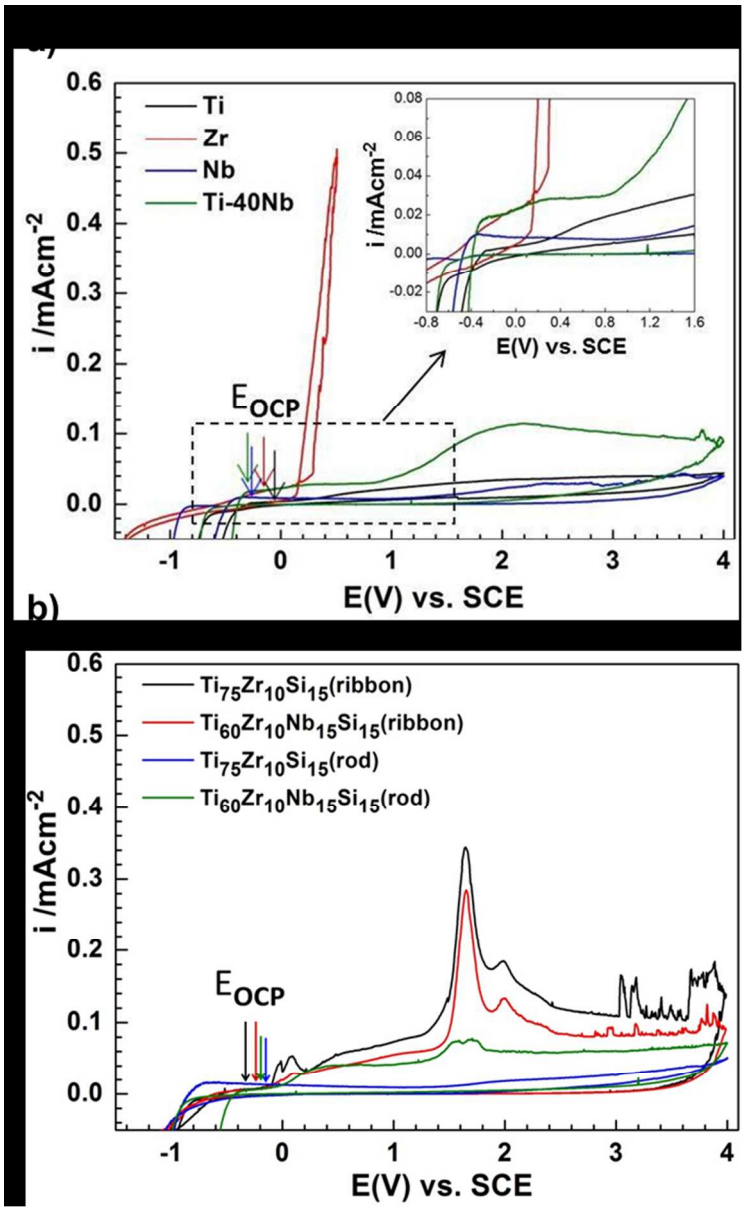

114x186mm (150 x 150 DPI)

a)

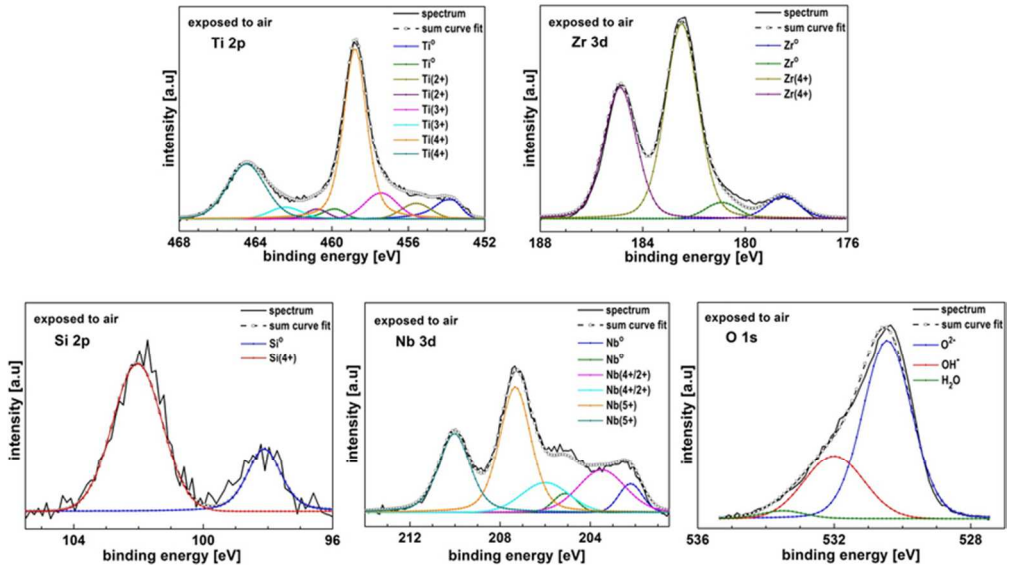

73x46mm (300 x 300 DPI)

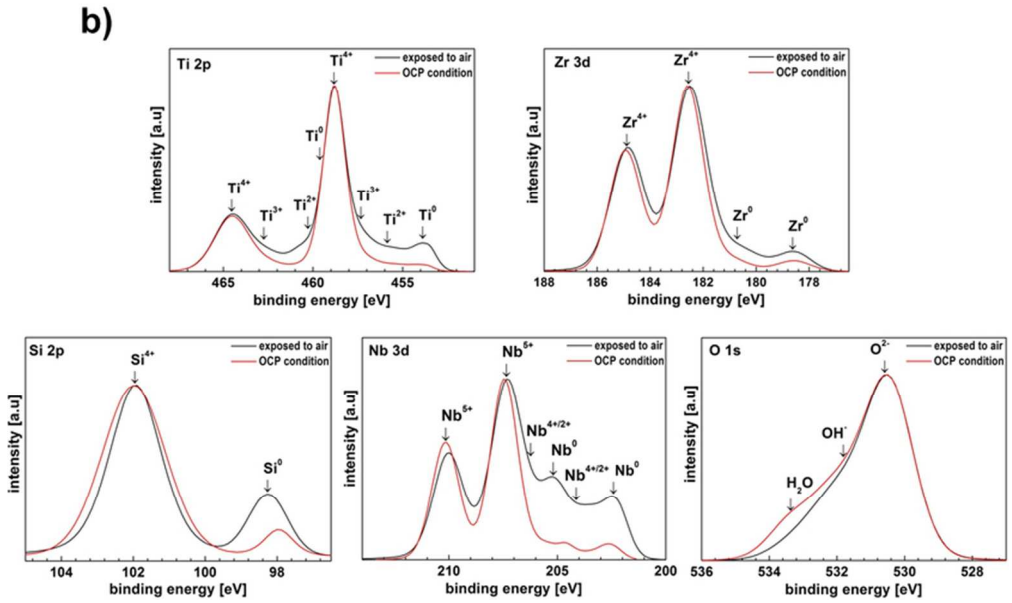

70x43mm (300 x 300 DPI)

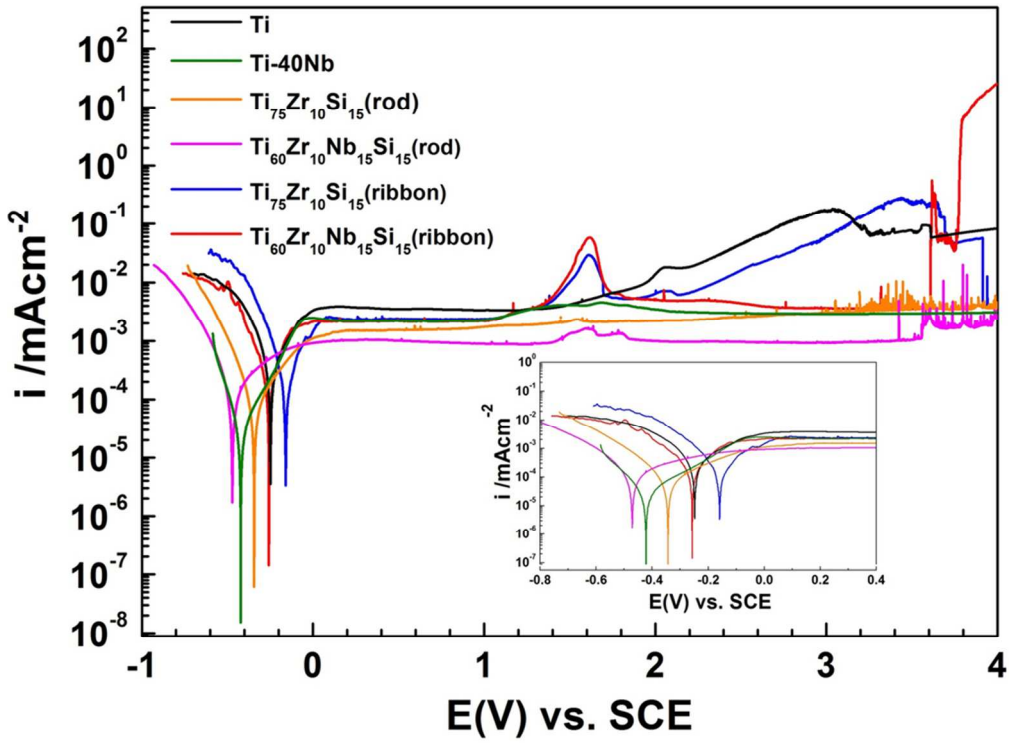

86x63mm (300 x 300 DPI)

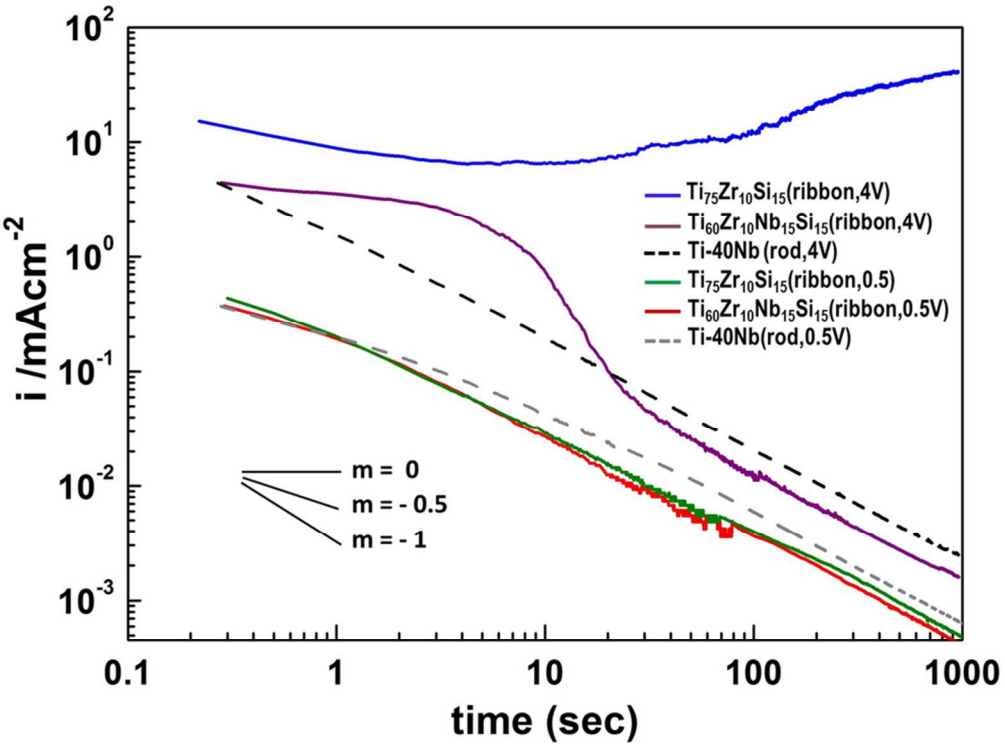

83x61mm (300 x 300 DPI)

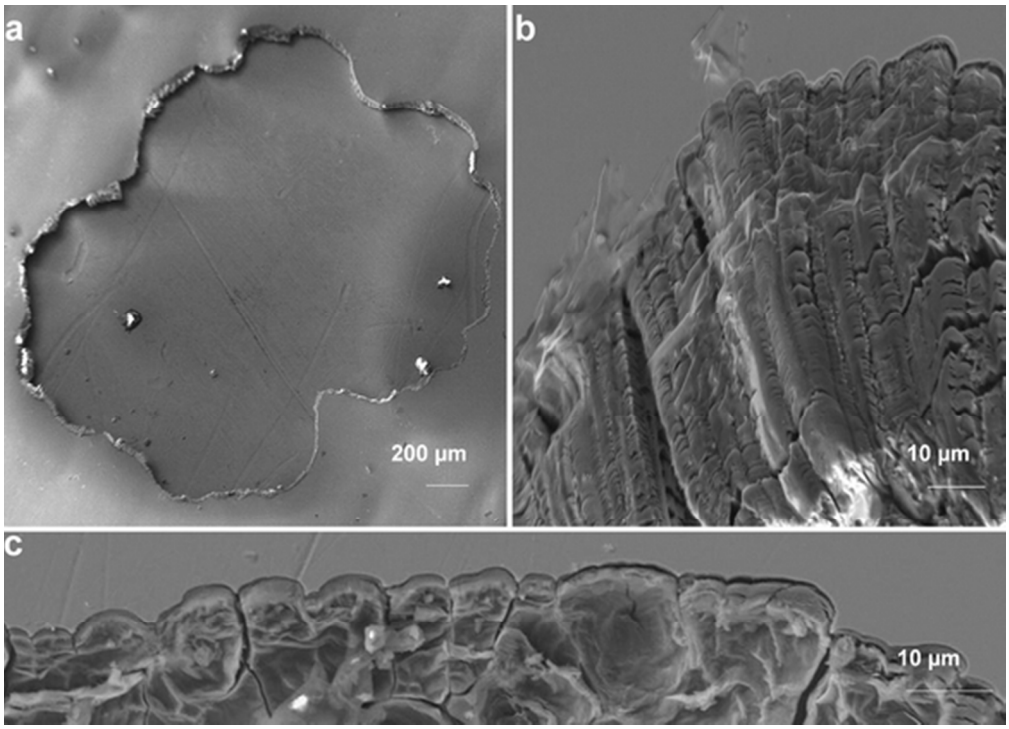

49x35mm (300 x 300 DPI)

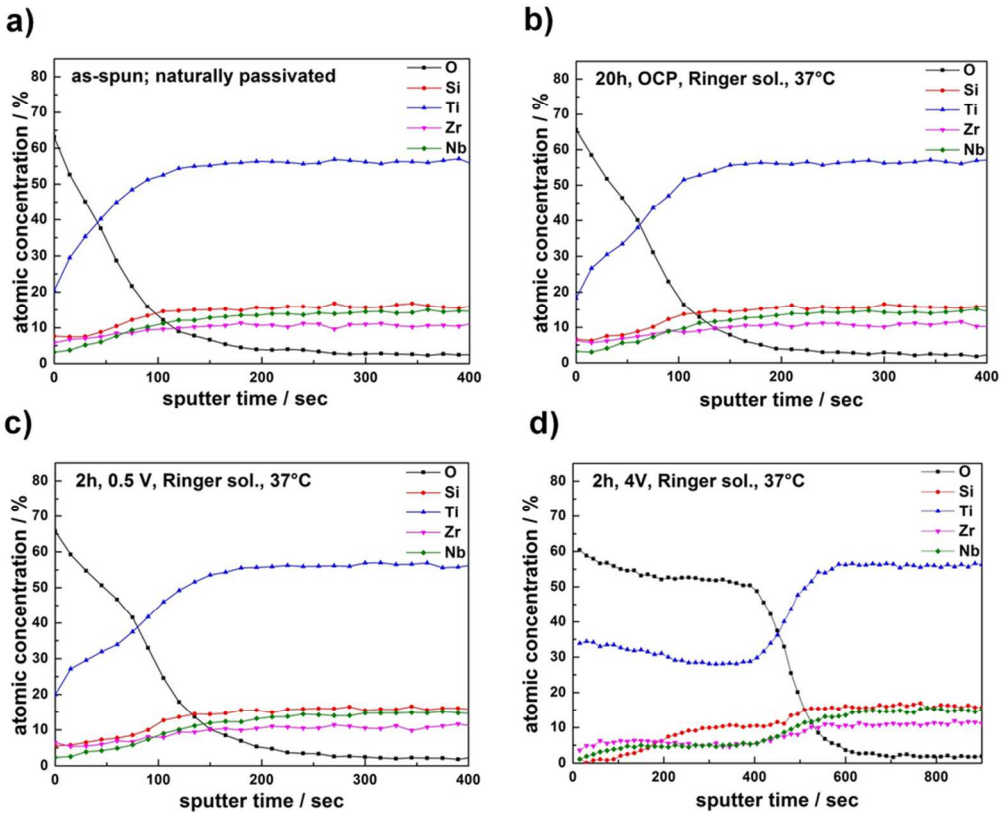

84x68mm (300 x 300 DPI)

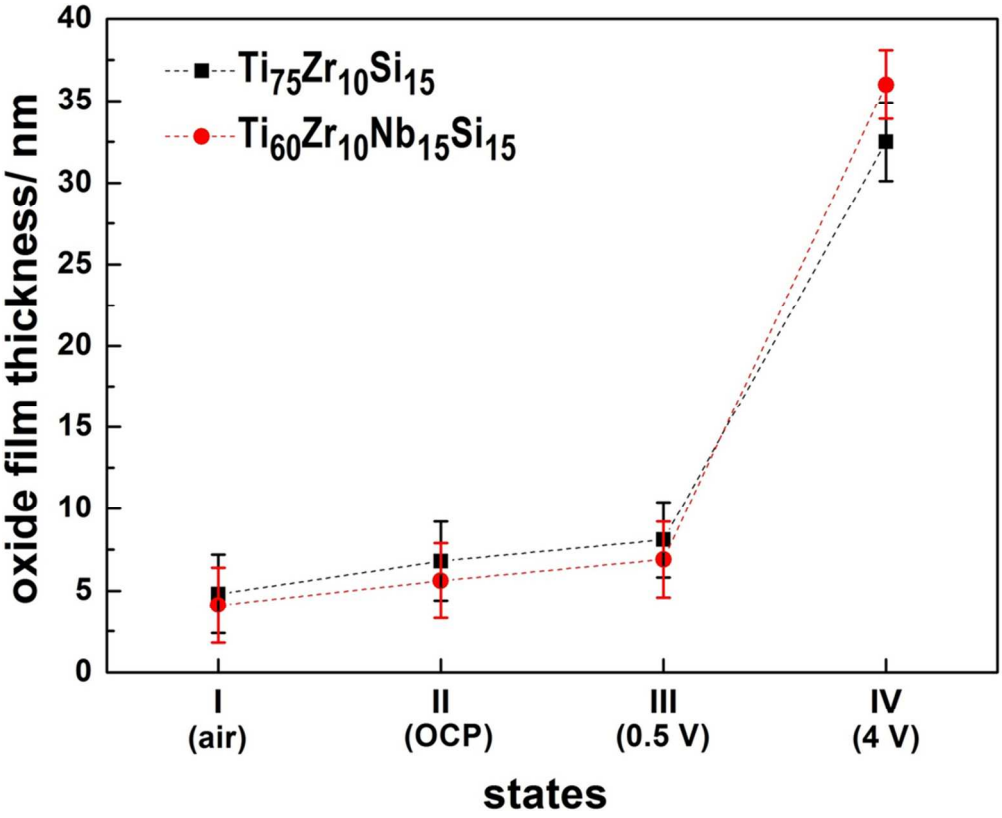

85x68mm (300 x 300 DPI)

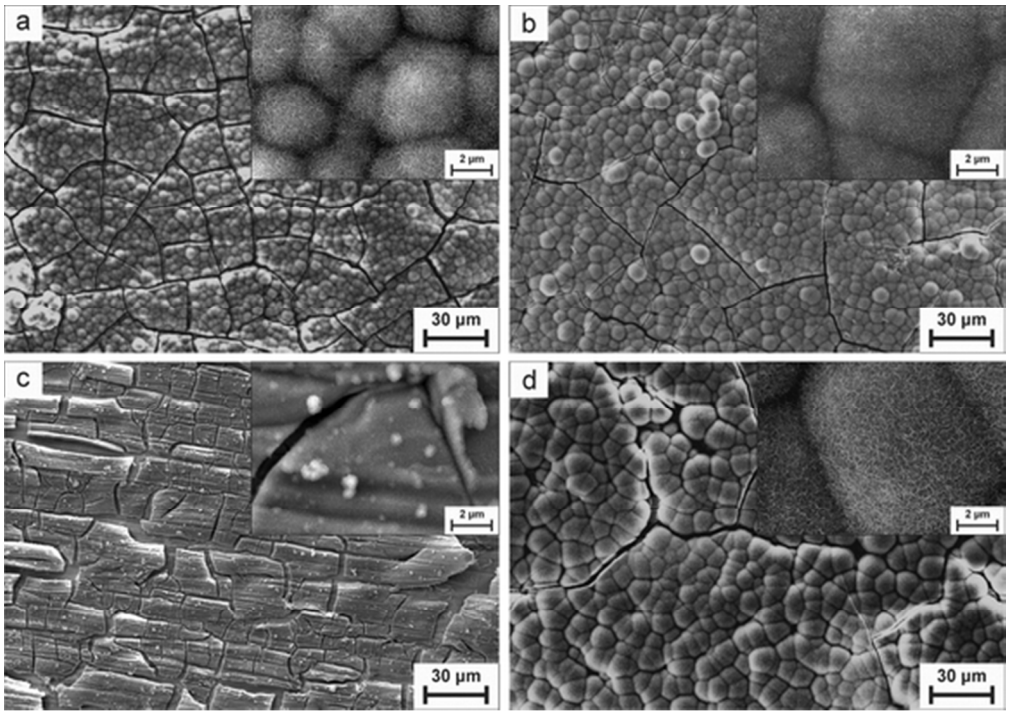

49x34mm (300 x 300 DPI)